Monthly Notices of the ROYAL ASTRONOMICAL SOCIETY

MNRAS **527,** 7767–7780 (2024) https://doi.org/10.1093/mnras/stad3631
Advance Access publication 2023 November 28

The superluminous Type IIn supernova ASASSN-15ua: part of a continuum in extreme precursor mass-loss

Danielle Dickinson [1,2★] Nathan Smith [2] Jennifer E. Andrews,[2,3] Peter Milne,[2] Charles D. Kilpatrick [4] and Dan Milisavljevic[1,5]

[1]*Department of Physics and Astronomy, Purdue University, 525 Northwestern Avenue, West Lafayette, IN 47907, USA*
[2]*Steward Observatory, University of Arizona, 933 North Cherry Avenue, Tucson, AZ 85721, USA*
[3]*Gemini Observatory/NSF's NOIRLab, 670 N. A'ohoku Place, Hilo, HI 96720, USA*
[4]*Center for Interdisciplinary Exploration and Research in Astrophysics (CIERA) and Department of Physics and Astronomy, Northwestern University, Evanston, IL 60208, USA*
[5]*Integrative Data Science Institute, Purdue University, West Lafayette, IN 47907, USA*

Accepted 2023 November 15. Received 2023 November 15; in original form 2023 February 9

ABSTRACT

We present a series of ground-based photometry and spectroscopy of the superluminous Type IIn supernova (SN) ASASSN-15ua, which shows evidence for strong interaction with pre-existing dense circumstellar material (CSM). Our observations constrain the speed, mass-loss rate, and extent of the progenitor wind shortly before explosion. A narrow P Cygni absorption component reveals a progenitor wind speed of $\sim$100 km s^{-1}. As observed in previous SNe IIn, the intermediate-width H α emission became more asymmetric and blueshifted over time, suggesting either asymmetric CSM, an asymmetric explosion, or increasing selective extinction from dust within the post-shock shell or SN ejecta. Based on the CSM radius and speed, we find that the progenitor suffered extreme eruptive mass-loss with a rate of 0.1–1 M$_\odot$ yr^{-1} during the $\sim$12 yr immediately before the death of the star that imparted $\sim 10^{48}$ erg of kinetic energy to the CSM. Integrating its *V*-band light curve over the first 170 d after discovery, we find that ASASSN-15ua radiated at least 3×10^{50} erg in visual light alone, giving a lower limit to the total radiated energy that may have approached 10^{51} erg. ASASSN-15ua exhibits many similarities to two well-studied superluminous SNe IIn: SN 2006tf and SN 2010jl. Based on a detailed comparison of these three, we find that ASASSN-15ua falls in between these two events in a wide variety of observed properties and derived physical parameters, illustrating a continuum of behaviour across superluminous SNe IIn.

Key words: circumstellar matter – stars: evolution – supernovae: general – supernovae: individual: ASASSN-15ua – stars: winds, outflows.

1 INTRODUCTION

Type IIn supernovae (SNe) are identified by relatively narrow H emission lines in their spectra (Schlegel 1990; Filippenko 1997), which are narrower than the broad P Cygni profiles typically seen in normal Type II-P events. Whereas the broad lines in normal SNe II-P arise from emission by the recombining fast ($\sim 10^4$ km s^{-1}) SN ejecta, the narrow emission in SNe IIn is typically a superposition of 'narrow-' ($\sim 10^2$ km s^{-1}) and 'intermediate-width' ($\sim 10^3$ km s^{-1}) components. The narrow emission component traces the dense photoionized gas in the pre-shock circumstellar material (CSM), and the intermediate-width emission can arise from either electron scattering (more common in early spectra) or from the accelerated post-shock gas (typically seen at later times). See Smith (2017) for a review of interacting SNe.

The progenitors of SNe IIn are believed to undergo extreme mass-loss events immediately prior to explosion. Observed mass-loss rates, inferred from optical light curves of SNe IIn and narrow/intermediate-width H α, are of the order of 0.01–1 M$_\odot$ yr^{-1} or more (Smith 2014, 2017), whereas steady radiation-driven stellar wind mass-loss rates are expected to be $\lesssim 10^{-4}$ M$_\odot$ yr^{-1} (Smith & Owocki 2006; Smith 2014). This suggests that an episodic or eruptive mechanism drives the pre-SN mass-loss to form dense CSM around SNe IIn, and comparisons have been made to the giant outbursts of luminous blue variables (LBVs) and SN imposters (van Dyk 2005; Smith et al. 2011a). Indeed, there are now several cases where an SN IIn was preceded by an observed eruption in the few years immediately before the SN (Smith et al. 2010a; Fraser et al. 2013; Ofek et al. 2014; Smith 2014; Bilinski et al. 2015; Elias-Rosa et al. 2016).[1] Sources of this eruptive mass-loss may arise from instabilities associated with advanced stages of nuclear burning, including the pulsational pair instability, wave driving, or other nuclear burning instabil-

★ E-mail: dickinsd@purdue.edu

[1]Note that we are not counting cases where a claimed precursor event may have been the SN itself before the onset of CSM interaction, and we are not including the first detection of a pre-SN event in the case of SN 2006jc's precursor (Pastorello et al. 2007) because it was a Type Ibn, not a Type IIn event.

ities (Woosley, Blinnikov & Heger 2007; Quataert & Shiode 2012; Shiode & Quataert 2014; Smith & Arnett 2014; Fuller 2017; Woosley 2017; Fuller & Ro 2018; Renzo et al. 2020; Woosley & Smith 2022), or violent LBV-like binary interaction events and pre-SN mergers (Smith & Arnett 2014; Smith et al. 2018, 2022; Schrøder et al. 2020).

SNe IIn exhibit wide diversity in terms of luminosity, inferred CSM mass, radial distribution of the CSM (and hence, timing of the mass-loss before explosion), and asymmetry (Smith 2017), but all require pre-SN mass-loss that is much stronger than what normal steady winds of massive stars can provide (Smith 2014). Among SNe IIn, the most extreme cases that produce the highest luminosity from CSM interaction are the so-called superluminous supernovae (SLSNe) that can reach absolute magnitudes ≤ -21 mag in the R band (Gal-Yam 2012).

The extreme luminosity of SLSNe IIn arises because of the ability of CSM interaction to efficiently convert SN ejecta kinetic energy into radiation, rather than because of extreme explosion energy (Smith & McCray 2007; van Marle et al. 2010; Chevalier & Irwin 2011). In other words, the unusual property of SLSNe IIn is related to CSM close to the star, rather than a highly unusual SN explosion. Most SLSNe are consistent with a normal (i.e. 10^{51} erg) explosion energy, and even the most extreme cases like SN 2006gy may only require an explosion energy of a few $\times$ 10^{51} erg (Smith et al. 2010b). On the other hand, SLSNe without narrow H lines in their spectra (Quimby et al. 2011) may derive their extreme luminosities from a different mechanism such as energy injection from a magnetar (Maeda et al. 2007; Kasen & Bildsten 2010; Woosley 2010).

Interacting SNe may greatly contribute to the dust budgets of high-redshift galaxies (Gall et al. 2014; Bevan et al. 2019; Niculescu-Duvaz et al. 2022). There are several observational signatures of new dust formation in SNe: (1) infrared (IR) excess, (2) increased fading rate of the optical flux, and (3) a progressive and systematic blueshifting of emission-line profiles, which is attributed to post-shock or ejecta dust formation that blocks line emission from the redshifted side of the explosion. An interacting SN's shock consists of the forward shock, the reverse shock, and a cold dense shell (CDS) that forms in between them (Chugai 2001; Smith et al. 2008b). Dust may form in this region due to efficient radiative cooling of post-shock gas collapsing into a thin, dense, and clumpy layer (Smith, Foley & Filippenko 2008a; van Marle et al. 2010). Several H-rich interacting SNe, including SN 2010jl (Smith et al. 2011b; Gall et al. 2014), SN 2017hcc (Smith & Andrews 2020), and SN 2005ip (Smith et al. 2009b; Bevan et al. 2019) have shown clear signatures of dust formation, most notably with their similar blueshifted line profiles. Dust masses for SN 2010jl and SN 2005ip have been estimated to be 0.005–0.01 $M_\odot$ (Bevan et al. 2020) and 0.1 $M_\odot$ (Bevan et al. 2019), respectively.

In this paper, we discuss the SLSN IIn event ASASSN-15ua (also known as PS16ub), which was first identified with a V-band magnitude of 16.9 mag by Masi et al. (2015) on 2015 December 12 (MJD $= 57368$, UT dates are used throughout this paper). ASASSN-15ua is located 0.95 arcsec south and 1.40 arcsec east from the centre of the host galaxy GALEXASC J133454.49+105906.7 (Masi et al. 2015). Its redshift of $z = 0.057 \pm 0.001$ indicates a distance of 256.3 Mpc, assuming $H_0 = 69.6$ km s^{-1} Mpc^{-1}, $\Omega_M = 0.286$, $\Omega_\Lambda = 0.714$ (Wright 2006). It was discovered on 2015 December 12 (MJD $= 57368$), while the first detection can be traced back to 2015 December 9 with a V-band magnitude of 17.5 mag. We correct for a foreground Milky Way and Host extinction of $A_V = 0.178$ mag, using $R_V = 3.1$ (Schlafly & Finkbeiner 2011), Milky Way $E(B-V) = 0.0247$ mag, and host $E(B-V) = 0.0331$ mag [see Section 2.3, $E(B-V)_{tot} = 0.0578$ mag]. The absolute magnitude at discovery then becomes $M_V = -20.32$ mag. ASASSN-15ua's spectra showed strong narrow emission lines attributed to CSM interaction at early times, indicating that it was a SN IIn event (Challis et al. 2015), and our continued spectral series shows narrow H emission persisting throughout its evolution.

We place ASASSN-15ua in context with the well-studied and seemingly distinct SNe IIn: SN 2006tf and SN 2010jl. The progenitors to both objects has been claimed to be LBV-like stars, but since LBV eruptions are an observed phenomenon without a well-understood physical cause, this does not directly address the underlying mechanisms for the pre-SN mass-loss. Characterizing the diversity of SNe IIn and their progenitors can help constrain the final stages of a massive star's life. We present our observations in Section 2. The light curve and spectral evolution are discussed in Section 3. Section 4 reviews our main results, assesses the CSM interaction strength and CSM mass requirements, and discusses them in the context of other luminous CSM interaction-powered SNe. A consistent theme is that in many respects, we find ASASSN-15ua to have observed characteristics and inferred physical properties intermediate between the two well-studied SLSNe IIn events SN 2006tf (Smith et al. 2008b) and SN 2010jl (Smith et al. 2011b, 2012; Zhang et al. 2012; Gall et al. 2014; Jencson et al. 2016).

2 OBSERVATIONS

2.1 Photometry

We obtained optical photometry of ASASSN-15ua in *BVRI* filters using the robotic 0.6 m Super-LOTIS (Livermore Optical Transient Imaging System; Williams et al. 2008) telescope located on Kitt Peak. Standard reductions, including flat-fielding and bias subtraction, were carried out using procedures described by Kilpatrick et al. (2016). Aperture photometry using Landolt catalogue in IRAF was performed on the reduced images. Table 1 lists the apparent magnitudes for the Super-LOTIS data.

We also measured optical *BVRI* photometry of ASASSN-15ua in images obtained with the Mont4k CCD Camera (Fontaine et al. 2014) mounted on the 1.5m Kuiper Telescope on Mt. Bigelow, Arizona. Flat-fielding and bias subtraction were performed using standard image calibration procedures. Template subtraction was performed on the Kuiper images by the High Order Transform of Psf ANd Template Subtraction code[2] with pre-explosion Pan-STARRS1 (PS1) images (Tonry et al. 2006). Aperture photometry using Landolt catalogue in IRAF was performed on the reduced images.

We also retrieved publicly available *grizyw* photometry from PS1 (Chambers et al. 2016; Flewelling et al. 2020) 3Pi Steradian Survey's Gigapixel Camera (Tonry et al. 2006). PS1 photometry are PSF magnitudes from template subtracted images using zero-points in the nightly processed 3Pi images, which are tied to the calibration in Schlafly et al. (2012) and Magnier et al. (2020). We retrieved optical photometry in V band from ASASSN (Shappee et al. 2014; Hart et al. 2023). These magnitudes were obtained with aperture photometry, with a median zero-point calibrated from the APASS Catalog.

One late-time (day 1267, 2019 June 1) r-band image of ASASSN-15ua was obtained using the imaging mode of Binospec (Fabricant et al. 2019), mounted on the 6.5 m MMT Observatory located on Mt. Hopkins, Arizona. This image is shown in the right panel of Fig. 1. At this late phase, it appears that the SN has faded beyond detection

[2]https://github.com/acbecker/hotpants, contributed by Andy Becker and Ira W. Snyder

Table 1. Super-LOTIS and Kuiper Photometry.

JD	*B* (mag)	*V* (mag)	*R* (mag)	*I* (mag)	Instrument
2457372.21	17.51 (0.04)	16.95 (0.02)	16.73 (0.03)	16.41 (0.03)	Super-Lotis
2457374.22	17.48 (0.06)	16.89 (0.04)	16.72 (0.07)	–	Super-Lotis
2457375.22	–	16.97 (0.02)	16.73 (0.02)	16.30 (0.04)	Super-Lotis
2457376.22	17.57 (0.07)	17.01 (0.04)	16.71 (0.06)	–	Super-Lotis
2457385.22	–	17.01 (0.02)	16.75 (0.03)	16.46 (0.04)	Super-Lotis
2457388.20	17.55 (0.11)	17.07 (0.04)	16.83 (0.04)	–	Super-Lotis
2457389.22	–	17.02 (0.01)	16.80 (0.01)	16.44 (0.02)	Super-Lotis
2457390.20	17.76 (0.04)	17.04 (0.02)	16.83 (0.02)	–	Super-Lotis
2457391.21	–	17.06 (0.01)	16.82 (0.01)	16.45 (0.02)	Super-Lotis
2457405.22	17.81 (0.05)	17.15 (0.02)	16.89 (0.03)	–	Super-Lotis
2457411.21	18.06 (0.15)	17.10 (0.05)	16.98 (0.06)	–	Super-Lotis
2457414.20	17.98 (0.15)	17.17 (0.09)	16.91 (0.09)	–	Super-Lotis
2457423.20	18.05 (0.05)	17.35 (0.03)	17.10 (0.04)	–	Super-Lotis
2457426.20	18.18 (0.05)	17.34 (0.02)	17.08 (0.03)	–	Super-Lotis
2457429.20	18.07 (0.04)	17.38 (0.02)	17.11 (0.02)	16.81 (0.03)	Super-Lotis
2457432.20	18.18 (0.04)	17.35 (0.02)	17.11 (0.02)	16.76 (0.03)	Super-Lotis
2457435.20	18.22 (0.05)	17.38 (0.03)	17.13 (0.03)	16.78 (0.03)	Super-Lotis
2457458.09	18.30 (0.06)	17.57 (0.04)	17.22 (0.05)	17.93 (0.29)	Super-Lotis
2457520.92	18.82 (0.12)	17.99 (0.05)	17.67 (0.04)	–	Kuiper
2457534.36	18.74 (0.07)	17.98 (0.07)	17.68 (0.08)	–	Kuiper
2457543.12	19.06 (0.26)	18.08 (0.06)	17.83 (0.05)	–	Kuiper
2458857.20	20.00 (1.46)	18.42 (1.47)	–	–	Super-Lotis
2458873.07	–	–	19.21 (0.09)	17.44 (0.44)	Super-Lotis

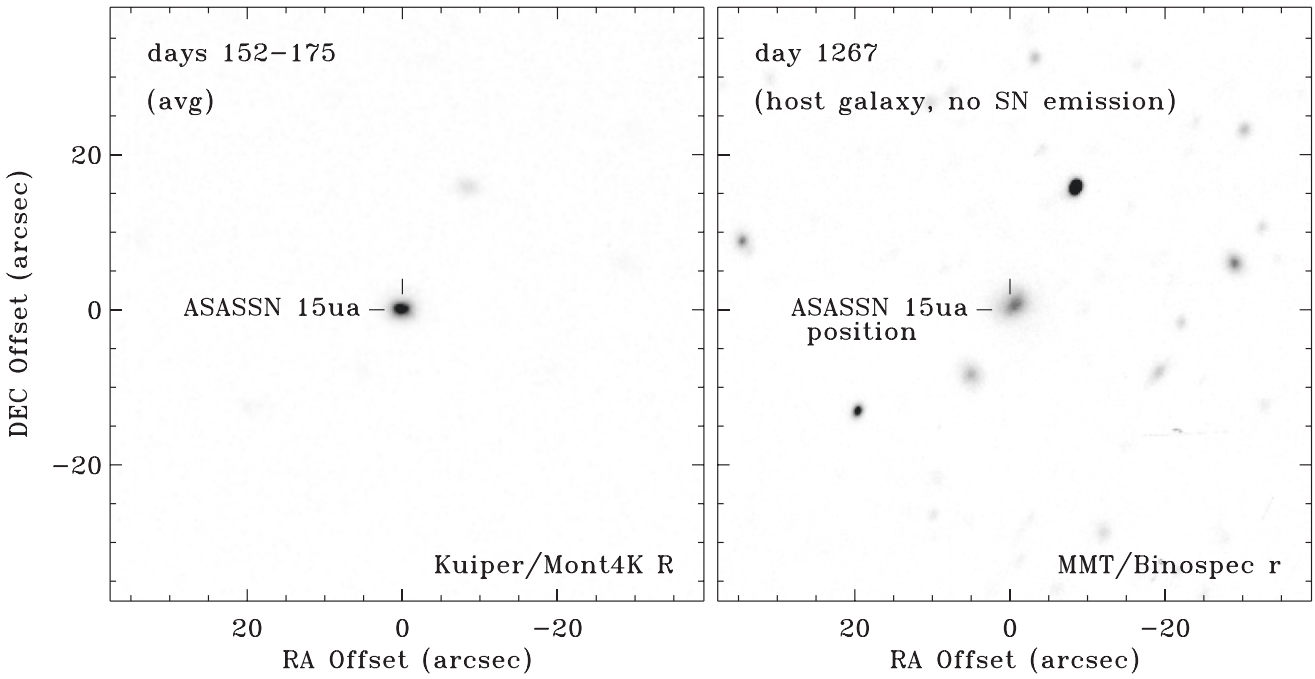

Figure 1. Images of the SN location with and without SN light. Left: Kuiper/Mont4k *R*-band image of ASASSN-15ua with the SN location identified. This is an average of three images taken between days 152 and 175 after discovery, when SN light still dominated the observed flux. Right: MMT/Binospec *r*-band image of the same field at late times after the SN faded, showing its location in its host galaxy GALEXASC J133454.49+105906.7 as measured in the Kuiper image in the left panel.

limits, as there is no residual flux in the template subtracted image. The very faint dwarf galaxy host of ASASSN-15ua is similar to that of SN 2006tf (Smith et al. 2008b), and relatively faint dwarf hosts seem to be a common property among SLSNe IIn (Stoll et al. 2011).

The multiband photometry of ASASSN-15ua is shown in Fig. 2. We take day 0 to be the discovery confirmation date, MJD = 57368, 2015 December 12. The data shown in Fig. 2 have not yet been corrected for extinction.

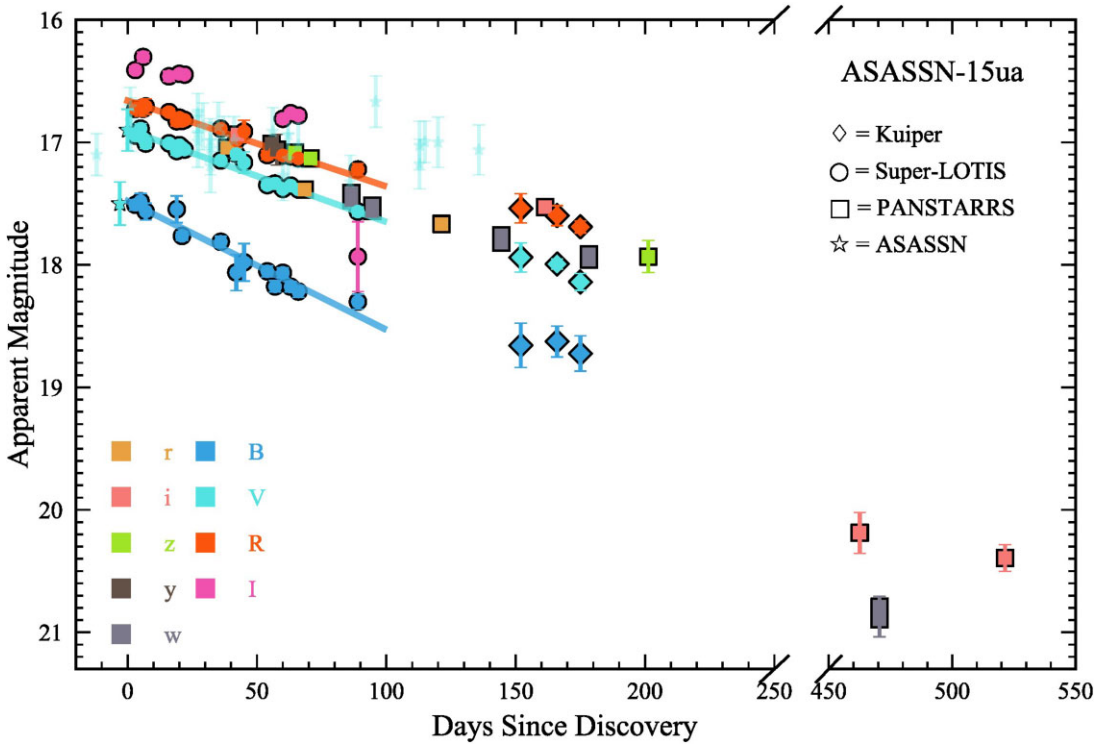

Figure 2. *BVRI* photometry from Super-LOTIS, PS1, and Kuiper (see Table 1) and *grizwy* photometry from PS1. These photometry are not corrected for extinction. Days since discovery is displayed because the time of explosion and time of peak are unknown; this is adopted for the remainder of the paper. The bulk of available photometry is in the first 170 d, which is shown on the left, while *i*- and *w*-band photometry are the only filters included at late times, shown at right. Diamond markers indicate Kuiper *BVR* data, circular markers indicate SL *BVRI* data, and squares indicate PANSTARRS *grizyw*. Slopes have been applied to *BVR* photometry to indicate time evolution in the first 100 d.

2.2 Spectra

During the 170 d after discovery, we obtained eight optical spectra of ASASSN-15ua, with observations summarized in Table 2 and the spectra plotted in Fig. 3. Five of the spectra were from the Bok 2.3m Telescope using the Boller & Chivens Spectrograph (B&C Spectrograph; Angel, Hilliard & Weymann 1979); the epochs for these spectra are 48, 68, 137, 157, and 179 d after discovery, with a 300 lines mm^{-1} grating, slit width of 1.5 arcsec, wavelength coverage of 3700–8000 Å (3200−7500 Å in rest wavelengths), and approximate resolution of 8 Å (365 km s^{-1} at Hα). Line measurements for the Bok spectra are provided in Table 3. The other three spectra had higher spectral resolution, and were obtained with the 6.5 m MMT using the Blue Channel Spectrograph, covering the epochs of 66, 175, and 453 d, obtained with the 1200 lines mm^{-1} grating that yielded a wavelength coverage of 5750–7000 Å (5400–6600 Å in rest wavelengths), and approximate resolution of 1.45 Å (66 km s^{-1} at Hα). The slit was oriented along the parallactic angle for all MMT and Bok observations.

2.3 Host Na I D Absorption

We marginally detect Na I D absorption due to the host galaxy in the higher resolution spectrum taken 66 d after maximum light (see Fig. 4). We measure the equivalent widths of Na I D_1 and D_2 to be 0.122 ± 0.031 and 0.162 ± 0.010 Å, respectively. Using equation (8) in Poznanski, Prochaska & Bloom (2012), we calculate a host $E(B-V) = 0.033 \pm 0.018$ mag. Adding this to the foreground Milky Way extinction quoted earlier, we adopt a total $E(B-V) = 0.058$ mag.

3 RESULTS

3.1 Light curve

Photometry obtained with Super-LOTIS, PS1, and Kuiper are shown in Fig. 2. Slopes are obtained by fitting to the *BVR* photometry for the first 100 d. The corresponding light curve decay rates are 0.011, 0.0075, and 0.0069 mag d^{-1}, respectively. While the decay rate of the *B*-band light curve is similar to the radioactive decay of ^{56}Co, the light curves in other bands decay more slowly, indicating that the bolometric luminosity decay is slower than ^{56}Co. This suggests that radioactive heating is not the only power source for the observed luminosity. The observed $B-V$ colour gets redder at a rate of 0.0031 mag d^{-1}.

Fig. 5 shows the absolute *V*-magnitude light curve of ASASSN-15ua covering its first 170 d after discovery. The two well-studied SNe IIn, SN 2006tf, and SN 2010jl are included for comparison. Note that the light curves of these two objects have been corrected for both distance and Milky Way extinction, following values in

Table 2. Spectroscopic observations.

Date	MJD	Day[a]	Tel./inst.	Range Å	Exposure s	Resolution Å (km s^{-1})
2016 Jan 29	57416.43	48	Bok/B&C	3900–8100	600	≈8 (365)
2016 Feb 16	57434.47	66	MMT/BC	5750–7000	600	1.45 (66)
2016 Feb 18	57436.46	68	Bok/B&C	3700–8000	1200	≈8 (365)
2016 Apr 27	57505.40	137	Bok/B&C	4000–8300	900	≈8 (365)
2016 May 17	57525.36	157	Bok/B&C	3700–8000	600	≈8 (365)
2016 Jun 4	57543.21	175	MMT/BC	5740–7000	600	1.45 (66)
2016 Jun 8	57547.32	179	Bok/B&C	3800–7600	600	≈8 (365)
2017 Mar 9	57821.46	453	MMT/BC	5740–7000	1200	1.45 (66)

[a]Day 0 is taken as the date of discovery.

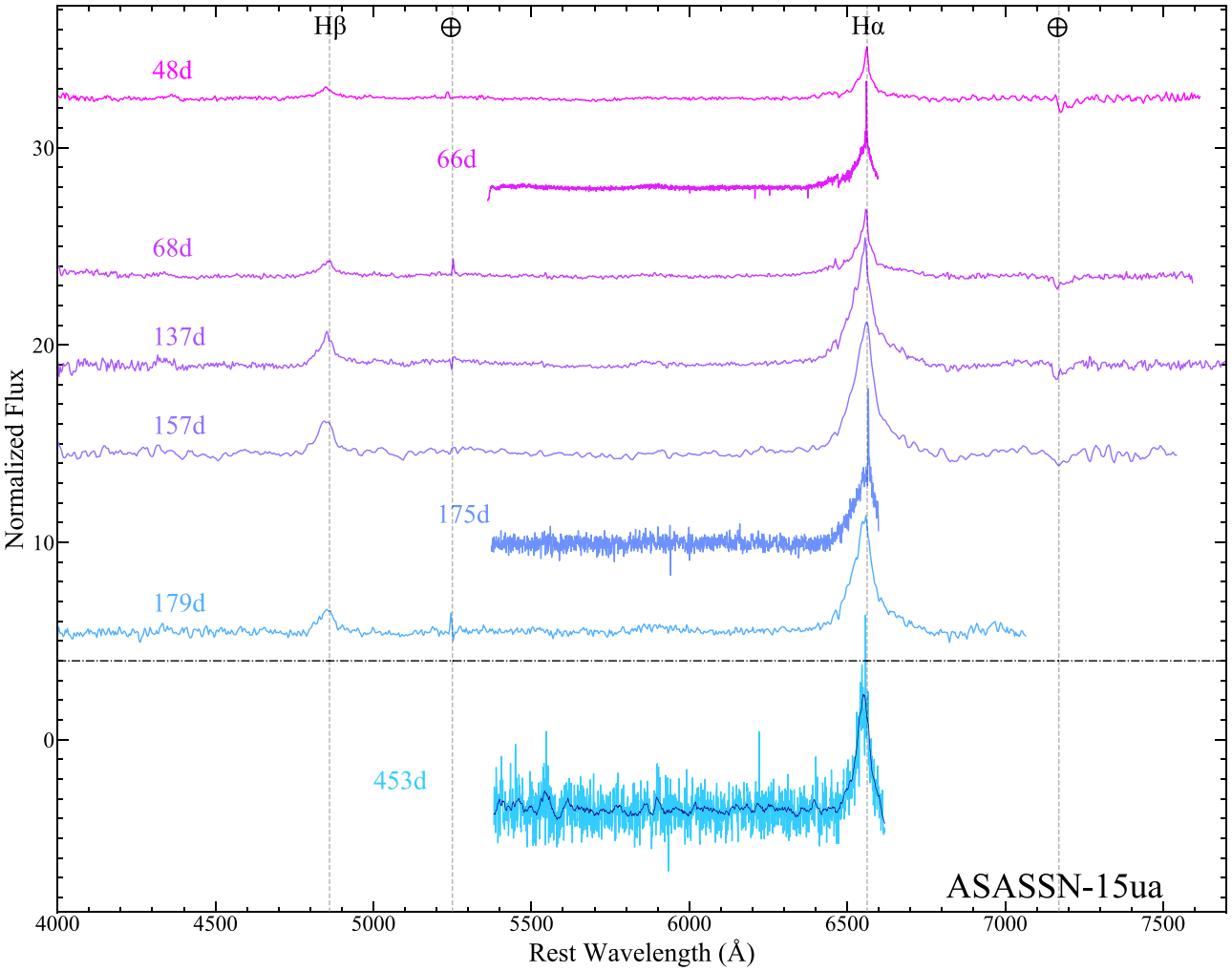

Figure 3. Visual wavelength, continuum-normalized spectra of ASASSN-15ua from Bok and MMT (see Table 2). The spectra on days 175 and 453 have been smoothed with 3 pixel bins. For day 453, an even further smoothed version of the same spectrum has been overlaid.

Smith et al. (2008b, 2011b). For SN 2006tf, we adopted $E(B-V) = 0.027$ mag (Smith et al. 2008b) and $d = 308$ Mpc (Quimby et al. 2007), and for SN 2010jl we adopted $E(B-V) = 0.024$ mag (Jencson et al. 2016) and $d = 46.5$ Mpc (host $z = 0.0107$, NED[3]).

[3]The NASA/IPAC Extragalactic Database (NED) is operated by the Jet propulsion Laboratory, California Institute of Technology, under contract with the National Aeronautics and Space Administration.

ASASSN-15ua is corrected for host and Milky Way extinction as described in Section 2.3. At early times, ASASSN-15ua's light curve resembles that of SN 2006tf in terms of its peak luminosity and rate of decline, although ASASSN-15ua appears to fade more slowly. In contrast, the plateaued decline of SN 2010jl slows after day 100 and maintains a high luminosity until about day 300. This implies that the radial distribution of CSM around ASASSN-15ua more closely resembles the compact configuration of SN 2006tf.

Table 3. Measurements of Balmer emission lines.

Date	MJD	Day[a]	EW (H α) Å	F (H α) 10^{-14} erg s^{-1} cm^{-2}	H α/H β
2016 Jan 29	57416.43	48	−172.84 (12.46)	5.02 (0.29)	2.21 (0.20)
2016 Feb 18	57436.46	68	−295.98 (13.11)	2.77 (0.17)	3.67 (0.30)
2016 Apr 27	57505.40	137	−592.16 (39.00)	4.87 (0.08)	4.38 (0.22)
2016 May 17	57525.36	157	−691.15 (30.46)	11.3 (0.3)	5.15 (0.19)
2016 Jun 8	57547.32	179	−546.44 (58.56)	5.97 (0.11)	4.29 (0.12)

[a]Day 0 is the date of discovery, MJD = 57368.

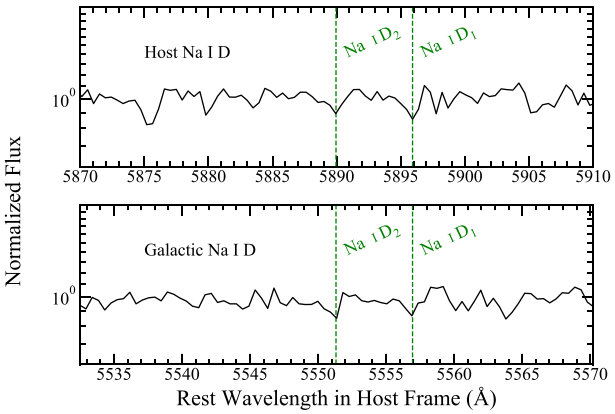

Figure 4. Na I D doublet in the day 66 MMT spectrum. In both panels, wavelengths have been corrected to show the rest wavelength at the redshift of ASASSN-15ua, and as a result, the Milky Way absorption components appear significantly blueshifted.

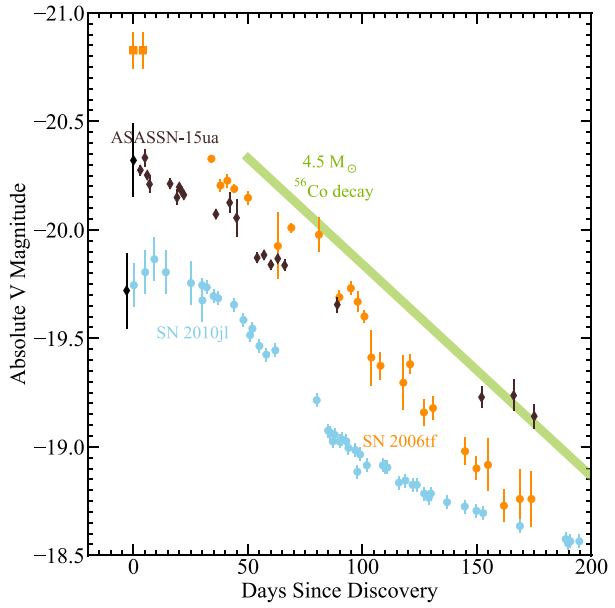

Figure 5. Absolute V-band magnitudes for IIn SLSNe: ASASSN-15ua, SN2006tf (Smith et al. 2008b), and SN2010jl (Stoll et al. 2011; Fransson et al. 2014). SN 2006tf and SN 2010jl have been adjusted to absolute magnitude adopting $E(B-V)$ values and distances described in the text. The squares are the unfiltered discovery observations of SN 2006tf. A slope corresponding to the radioactive decay rate consistent with 4.5 $M_\odot$ of ^{56}Co is shown for comparison.

Integrating the V-band light curve over the 170 d after discovery, we measure a total radiated energy of $E_{\rm rad} \sim 3 \times 10^{50}$ erg, which is not unusual for SLSNe. We did this by integrating a Gaussian process regression model (Garretson 2021) of the V-band photometry from 3 to 174 d. Note that this is an underestimate of the true value of $E_{\rm rad}$ because ASASSN-15ua was discovered at peak luminosity or after. The early rise to peak was largely missed, the late-time tail is not included, and we have made no bolometric correction (BC) to the optical light curve (there may be a significant BC at early times when the effective temperature is hotter). With these considerations, the total $E_{\rm rad}$ is likely to be around 10^{51} erg.

Fig. 5 includes a thick green slope indicating the expected decline rate for radioactive decay of 4.5 $M_\odot$ of ^{56}Co. Day 0 for SN 2006tf was determined using unfiltered discovery observations that measured $M_r = -20.7$ mag. Day 0 for SN 2010jl is the day of discovery. The V-band light curve of ASASSN-15ua declines more slowly than the trend expected for radioactive decay, making it unlikely that its light curve is dominated by a large mass of ^{56}Co. Instead, CSM interaction powers the luminosity, given the spectral signatures of ASASSN-15ua, as is the case with most SLSNe IIn. We use the luminosity and radiated energy of ASASSN-15ua to constrain its total CSM mass and progenitor mass-loss rate below, after we consider expansion speeds of the SN and CSM indicated by spectra.

3.2 Low-resolution spectra

In our analysis of spectral evolution, we will primarily consider the spectra obtained from the Bok telescope, as the MMT spectra have limited wavelength range. ASASSN-15ua has such a high redshift that the H α line resides near the edge of the observed wavelength range used for the MMT observations, unfortunately truncating the red wing of the line. The higher resolution MMT spectra are therefore used primarily to investigate the narrow P-Cygni lines arising from pre-shock CSM (see Section 3.3).

3.2.1 Line profile decomposition

The profile of Balmer lines in SNe IIn is complicated. At early times, electron scattering in the dense CSM broadens the narrow component into an intermediate-width profile with a Lorentzian shape (Chugai 2001). This profile usually evolves into a sum of two (or three) Gaussians, as the optical depth of the CSM drops and emission from the post shock gas (and sometimes also SN ejecta) is directly observable (Smith et al. 2008b; Smith 2017).

We compared three possible functions to the observed H α profile of ASASSN-15ua for each epoch of our Bok spectra (shown in Fig. 6 are only days 48 and 157). The first function is comprised of three Gaussians centred at 0 km s^{-1} with widths corresponding to the narrow-, intermediate-, and broad-width components. Due to progressive blueshifting of the line, these Gaussians were

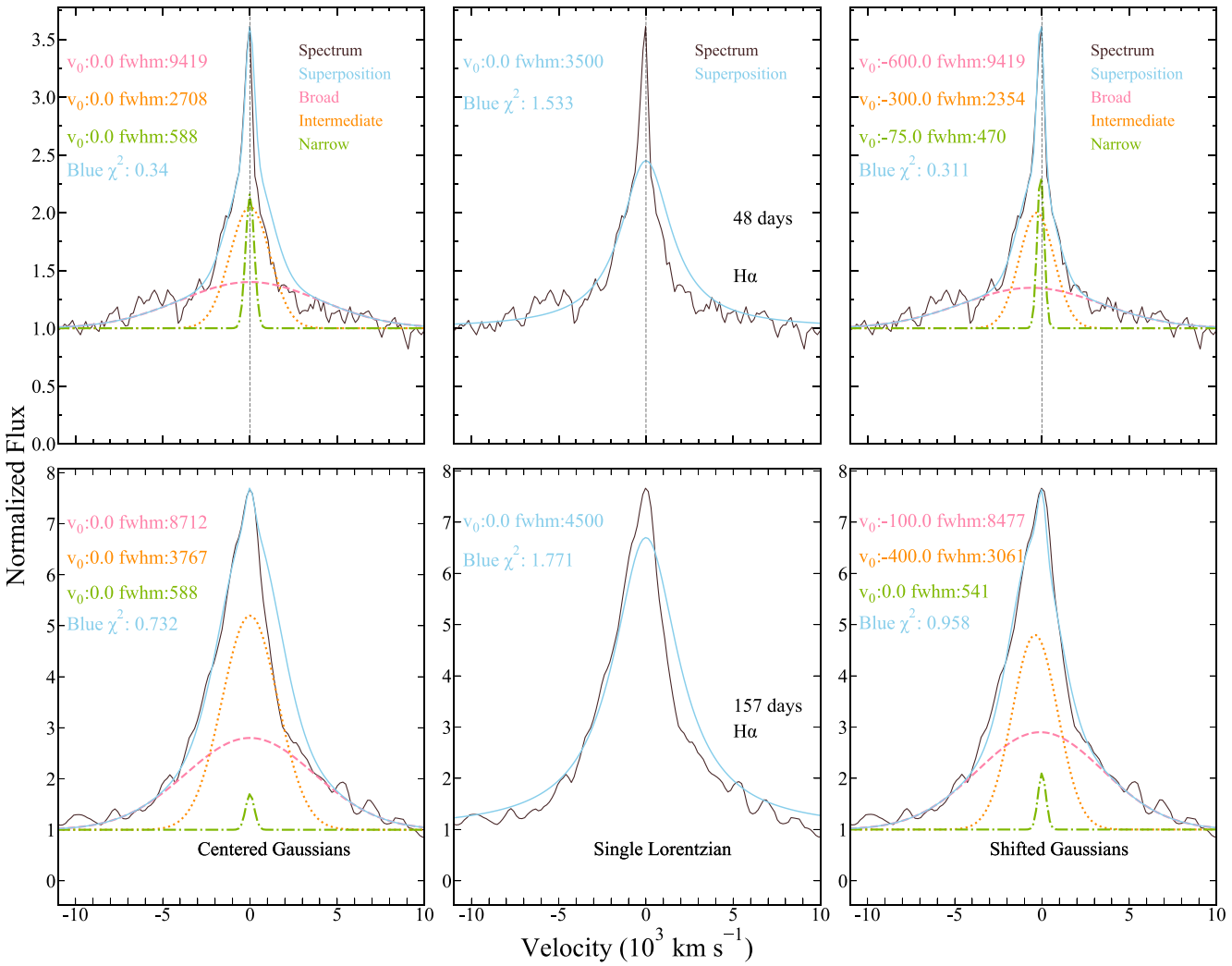

Figure 6. Various functions plotted against the H α profile in the Bok spectra observed on days 48 and 157. *Left*: Three Gaussians of varying width centred at 0 km s^{-1}, the centre of the narrow H α component. Gaussians have been fitted to the blueshifted side of the line, since the profile is asymmetric. *Centre*: A single Lorentzian centred at 0 km s^{-1}. *Right*: Three Gaussians of varying width shifted with respect to the centre of the line. The three Gaussians represent the broad, intermediate, and narrow components of the complex line profiles. The χ^2 of each function is listed; this value represents only the goodness of fit between the data and function on the blue side of the line.

only compared to the shape of the blue side. The second is a single Lorentzian representing an electron-scattered intermediate-width component. The last is three Gaussians where the centroids were allowed to shift to arbitrary nonzero values. This function aims to describe the whole shape of the complex line profile.

Fig. 6 shows these comparisons for days 48 and 157 (similar comparisons were made for all the Bok spectra but are not shown here). It is clear from the centre column that the shape of H α is never Lorentzian after 48 d. Across all epochs, the Lorentzian cannot describe the red side of the line. By day 48, most of the CSM is evidently no longer optically thick to electron scattering. We cannot well constrain the time of explosion, so the SN may be older than 48 d at that time, and hence, it is likely that none of our spectra captured the early-time behaviour.

The H α line is better described by three Gaussians. The broad component of both the centred and shifted Gaussians are generally similar in width for each epoch. The intermediate-width component of the centred Gaussians are systematically broader than their shifted counterparts, since they ignore the red wing of the line. The narrow components of both Gaussians do not show a clear trend, but it may be difficult to capture the narrow, 100 km s^{-1}, component because it is unresolved (resolution $\sim$ 600 km s^{-1} at H α) and blended with broader components. No obvious trend is seen in the zero-point velocity of any Gaussian curves in the shifted column, except that all non-zero shifts are to the blue. We suggest that it makes more physical sense for the centred Gaussian curves to describe the shape of the line, acknowledging that the red side of the line may be suppressed due to extinction from dust in the ejecta or CDS.

As these fits are not unique, nearly identical superpositions of the Gaussians could be produced with components of slightly different widths and strengths. What is shown here attempts to employ components as narrow and as strong as possible, guided by widths of components often observed in SNe IIn.

The intermediate- and broad-width components help guide our estimates for the expansion speed of the post-shock CDS and the SN ejecta, respectively. We adopt a shock speed of 2500 km s^{-1}.

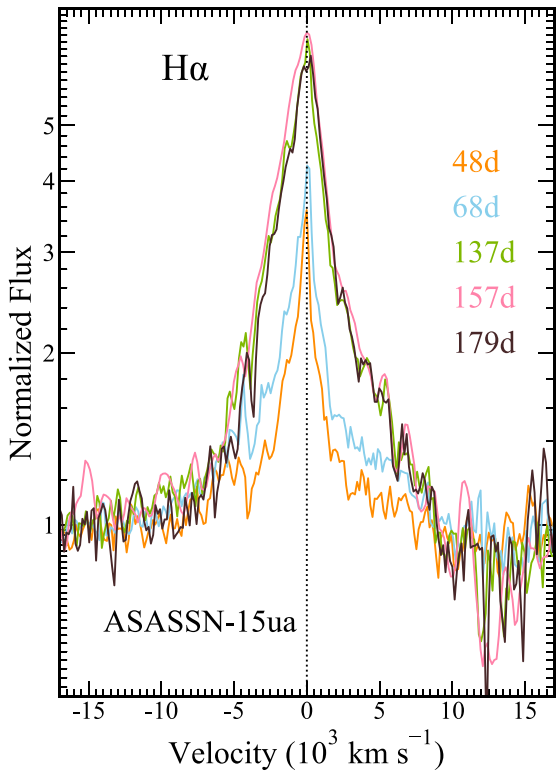

Figure 7. Evolution of the Hα line-profile shape seen in continuum-normalized Bok spectra of ASASSN-15ua. Note that the line core (a mix of the intermediate-width and unresolved narrow components at this resolution) becomes broader with time, but the blueshifted wing stays approximately the same.

The speed of the SN ejecta is observed to be of the order of 4000–5000 km s^{-1}. We will adopt CSM speeds from the day 66 P Cygni profile, discussed later (see Section 3.3).

3.2.2 *Line asymmetry and evolution*

Fig. 7 emphasizes the intermediate-width Hα profile on days 48, 68, 137, 157, and 179. The spectra are continuum-normalized. The classic Lorentzian electron-scattering shape of the emission, often seen in early-time spectra of SNe IIn, is not seen in ASASSN-15ua (see Section 3.2.1). Over time, we see the three characteristic widths of Hα emission in SNe IIn. All three components strengthen with time compared to the continuum. The widths of the narrow and broad component stay roughly constant, while the intermediate component becomes progressively blueshifted (recall that the narrow component is unresolved in these Bok spectra, but see Section 3.3 for a look at narrow component evolution).

The component spanning $\pm$2000 km s^{-1} accounts for the majority of the flux and dominates the overall appearance of the line profile. There is a sudden widening in the intermediate component of the spectra after 100 d. At each epoch, the blueshifted wing is stronger than the opposite side, as shown in more detail in Fig. 8. This figure shows the full observed Hα line profile (black) but also shows a mirrored version of the blue wing of the line, reflected over to the red side to demonstrate what the line profile would look like if it were symmetric. The blue wing reflected over to redshifted velocities is shown as a lighter, thicker line. Fig. 8 clearly demonstrates the asymmetry in the Hα profile, but it indicates the flux deficit on the redshifted wing is rather mild in ASASSN-15ua at these early phases.

At early times (48 and 68 d), the broad- and intermediate-width components are blueshifted, but the broad component becomes symmetric after 100 d. The asymmetry only persists in the intermediate-width component. This is clearer in the centred Gaussian curves in Fig. 6. The narrow component is fairly symmetric in all epochs, and the intermediate-width profile is systematically blueshifted, with an average shift of -350 ± 100 km s^{-1}. This could indicate early dust formation primarily in the post-shock gas.

3.2.3 *Line strengths and widths*

Our measurements of the time evolution of the equivalent width (EW) of Hα are plotted in Fig. 9, where the Hα EW of ASASSN-15ua is again compared to values for SN 2006tf and SN 2010jl. ASASSN-15ua is clearly intermediate between the two other SNe IIn, as the line strength increases with time. These values are positive for emission and include the total line emission from the narrow-, intermediate-, and broad-width line components. The Hα/Hβ line flux ratio is also compared to the ratio observed for SN2006tf and SN2010jl.

Since EW is a measure of line flux relative to the continuum flux, epochs with brighter continuum emission will tend to result in a smaller EW. As the continuum fades through time, the EW of Hα increases, as seen in Fig. 9. This is a common property of SNe IIn where the luminosity is dominated by CSM interaction (Smith, Mauerhan & Prieto 2014; Smith 2017). ASASSN-15ua's Hα EW evolution is similar in value and slope to SN 2010jl; if the post-shock gas in both objects cools at the same rate, this suggests that the CSM density profiles in ASASSN-15ua and SN 2010jl are similar. SN 2006tf has a lower EW due to additional continuum luminosity from delayed photon diffusion in its opaque shocked shell (Smith et al. 2008b).

The line flux ratio between Hα and Hβ, seen in Fig. 9 (right panel), shows all three objects increasing at similar rates during the main peak of the light curve. Note that due to the uncertain explosion epochs of both ASASSN-15ua and SN 2006tf, the horizontal offsets between the three SNe in this plot are uncertain, but ASASSN-15ua and SN 2006tf will only shift to the right, allowing more time to elapse between explosion and discovery. The time of maximum light in SN 2010jl is well-constrained, since its rise was captured.

At early times, the Hα and Hβ emission appear to be dominated by recombination after photoionization, with a line ratio close to a value of $\sim$3. At later times, the ratio rises to much larger values, incompatible with recombination emission. ASASSN-15ua evolves similarly to the two comparison SNe IIn but it seems to have a systematically smaller ratio at each epoch. Since all three SNe produce a Hα/Hβ ratio much larger than 3, the emission is dominated by collisional excitation (see section 5.5 in Smith et al. 2008b for more information), and the CSM is optically thin.

3.3 Narrow P Cygni absorption

Fig. 10 shows the relatively high-resolution MMT/Bluechannel spectra of ASASSN-15ua on days 66 and 175 after discovery. Both epochs exhibit narrow P Cygni absorption, although the velocity of this absorption changes. On day 66, the narrow P Cyg absorption trough minimum is at -85 ± 10 km s^{-1} with a blue edge at

-100 ± 10 km s^{-1}. On day 175, however, the narrow P Cyg absorption appears shallower and broader, with a trough centred at roughly -95 ± 10 km s^{-1} and a blue edge at -150 ± 50 km s^{-1}. Judging by the narrow absorption at early times and the narrow emission at both epochs, we adopt a pre-shock CSM expansion speed of 100 ± 10 km s^{-1} in our analysis. We note, however, the shift in P Cyg absorption to somewhat higher velocity at the later epoch might indicate a CSM with either a varying outflow speed, or an impulsive mass ejection that created a Hubble-like flow (i.e. where faster ejecta from the same pre-SN eruption have travelled to farther radii in the CSM, and therefore get overtaken at a later epoch by the shock).

4 DISCUSSION

4.1 Mass-loss history

In this section, we use observed properties of ASASSN-15ua to infer the mass-loss rate of the progenitor and approximate duration of enhanced mass-loss prior to explosion.

We use the narrow emission and absorption as an indicator of the expansion speed for the pre-SN mass-loss. Narrow P Cygni absorption of Hα can be seen in the high-resolution MMT spectra taken on days 66 and 175. These narrow features are shown in Fig. 10 alongside spectra of SN 2010jl and SN 2006tf. The shape of the P Cygni profile is well resolved on day 66, so we take the speed of the absorption's blue edge, $\sim$100 km s^{-1}, as the speed of the CSM on that day. A hot pixel or cosmic ray residual was present in the day 175 MMT spectrum within the apparent P Cygni absorption trough. This was carefully corrected from the 2D spectrum before extraction, but we nevertheless regard the resulting P Cygni absorption on day 175 with caution. We thus adopt 100 km s^{-1} for the CSM speed at the epoch, assuming constant CSM speed from early to late times. The width of the narrow component on day 175 appears wider than day 66, as can be seen from Fig. 10. The CSM speed immediately ahead of the shock may be increasing over time as the forward shock marches outward through faster material at larger radii, hence the apparent acceleration from 85 to 95 km s^{-1}. Nevertheless, we adopt a constant CSM speed of 100 ± 10 km s^{-1}, as this change (10 km^{-1}) in CSM speed would only modify $\dot{M}$ by 10 per cent, which falls under our uncertainty in the measurement and is far under the spectral resolution, 66 km s^{-1} at Hα.

For the speed of the forward shock, which is often traced by the intermediate-width component of Hα emission from the CDS, we adopt an approximate value of 2500 km s^{-1}. This choice is somewhat slower than the FWHM values of the intermediate-width components at later times in Fig. 7, but we chose a somewhat lower value because these lines may be partly blended with the broad component from SN ejecta (note that the intermediate-width component's FWHM value in the left column of Fig. 7 increases at late times, even though we might expect the shock to slow down), and lower values are more commonly seen in the shock speeds of other SNe IIn, which are typically between 2000 and 3000 km s^{-1} (Smith et al. 2008b; Jencson et al. 2016; Smith & Andrews 2020).

Assuming that the observed SN luminosity is dominated by CSM interaction, the mass-loss rate of the progenitor that would have been required to produce the dense CSM is given by

$$\dot{M}_{\rm CSM} = 2L \frac{V_{\rm CSM}}{(V_{\rm shock})^3}, \quad (1)$$

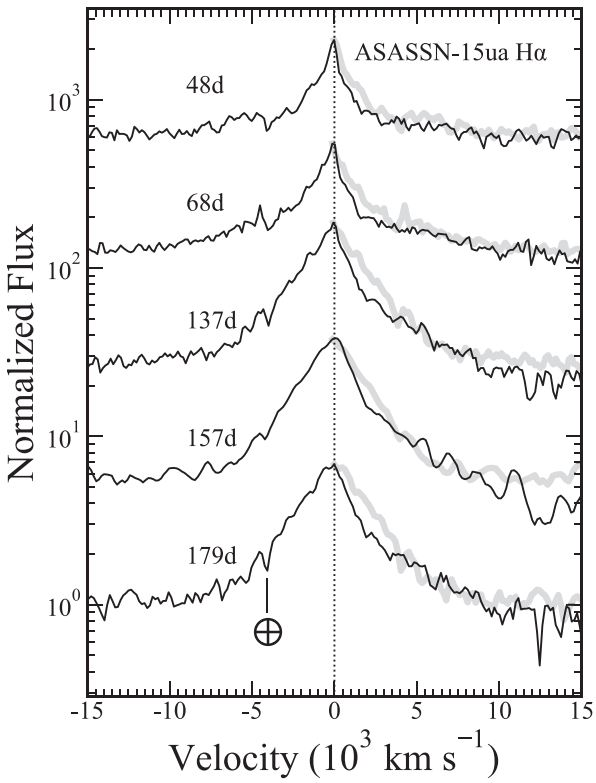

Figure 8. The same Hα line profiles as in Fig. 7 but separated vertically. This plot shows the blueshifted wing of the line reflected over (shown in a thicker line) to redshifted velocities. There is a consistent flux deficit on the observed redshifted wings, even though the narrow line peak is at zero velocity.

where equation (1) (Smith et al. 2008b)[4] calculates the progenitor mass-loss rate as a function of the observed CSM-interaction luminosity (L), shock speed ($V_{\rm shock}$), and pre-shock CSM speed ($V_{\rm CSM}$). The luminosity used is the R-band magnitude corrected for extinction at each epoch. This estimate assumes that the observed R-band luminosity traces 100 per cent of the CSM interaction luminosity. Since some of the CSM interaction luminosity may escape at other wavelengths (e.g. X-rays), this value of L – and hence the corresponding value of $\dot{M}$ – are lower limits.

In addition to quantifying the progenitor mass-loss rate, we can determine the approximate time prior to explosion when the CSM was ejected. We can leverage the ratio between $V_{\rm shock}$ and $V_{\rm CSM}$ and $t_{\rm SN}$, the time of observation, assuming constant $V_{\rm shock}$. The consequent equation is as follows:

$$t = t_{\rm SN} \frac{V_{\rm shock}}{V_{\rm CSM}}, \quad (2)$$

where the pre-SN ejection time of the CSM, t, is really a lower limit, because the observed value of $t_{\rm SN}$ is taken as the observed time, whereas the true explosion time was earlier than our day 0 and because we assume that the shock does not decelerate, which may occur as it encounters CSM. We find that ASASSN-15ua underwent extreme mass-loss at a rate of roughly 0.4 M$_\odot$ yr^{-1} for at least 12 yr

[4]Note that this quantity is very sensitive to a choice in v_{shock} as $\dot{M} \propto v_{shock}^{-3}$. However, regardless of shock speed within a reasonable range, the calculated mass-loss rate is always intermediate to SN 2006tf and SN 2010jl.

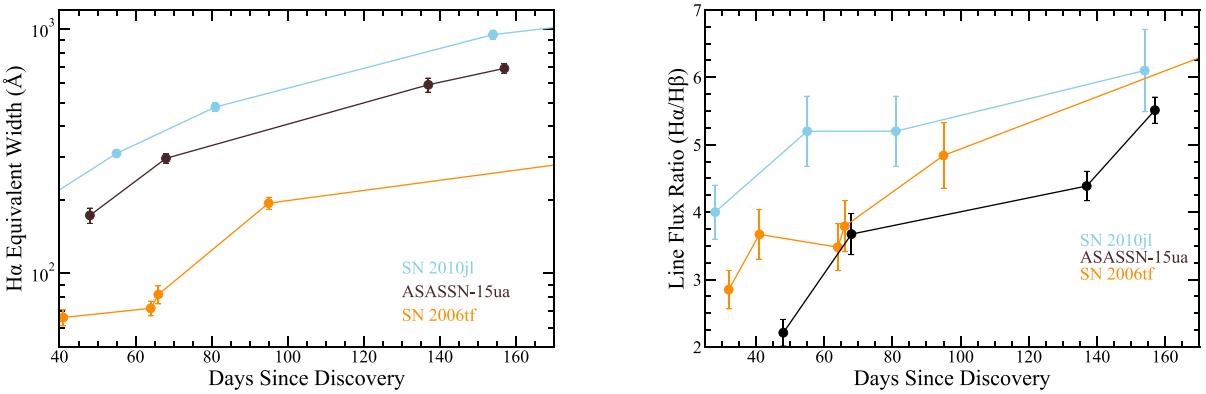

Figure 9. Left: Equivalent width (EW) of ASSASN-15ua's H α line, as well as the H α EW of SN 2010jl (Jencson et al. 2016) and SN 2006tf (Smith et al. 2008b). Right: Flux ratio of H α/H β for ASASSN-15ua, SN2010jl (Jencson et al. 2016), and SN2006tf (Smith et al. 2008b). The fluxes and ratios were measured from dereddened spectra, with $E(B-V)$ values for each SN noted earlier. Measurements for day 453 were omitted due to insufficient signal to noise.

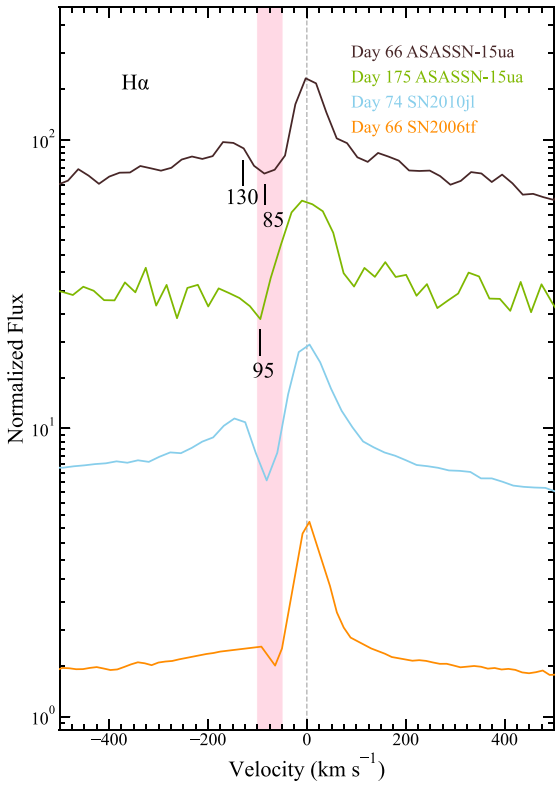

Figure 10. The narrow P Cygni profile of H α on days 66 and 175 compared to SN 2010jl and SN 2006tf on days 62 and 64, respectively.

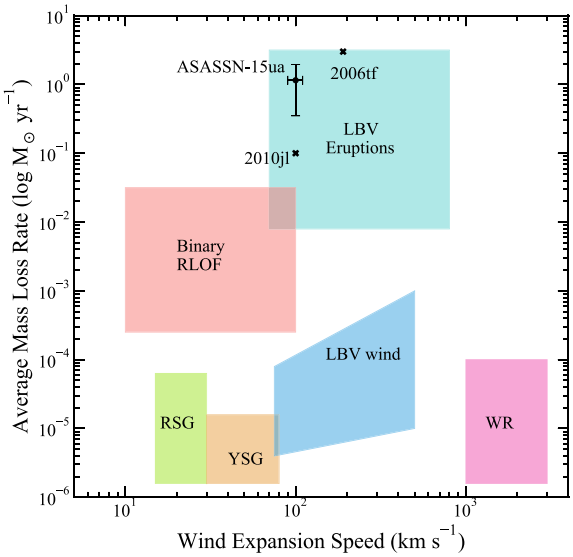

Figure 11. Constraining ASASSN-15ua's progenitor in mass-loss rate–wind velocity space. This is adapted from Smith (2017). SN2010jl and SN 2006tf have been marked on this plot as well.

prior to explosion, with an even higher rate of 0.7 $M_\odot$ yr^{-1} within 4.5 yr prior to explosion. The SN progenitor ejected a total of at least 6 $M_\odot$ of stellar material into the circumstellar environment, and moving at ∼100 km s^{-1}, carried a kinematic energy of 6×10^{47} erg. In this model, photons are emitted instantly from the post-shock gas.

The progenitor of SN 2006tf had been experiencing mass-loss at a rate of 0.1 $M_\odot$ yr^{-1} in roughly a century before explosion, but then increased to 2–4 $M_\odot$ yr^{-1} in the decade prior to eruption (Smith et al. 2008b). The eruptive mass-loss of SN 2010jl occurred over about 30 yr prior to eruption at a constant 0.1 $M_\odot$ yr^{-1}. Fig. 11 is adapted from Smith (2017) and includes the three objects ASASSN-15ua, SN 2006tf, and SN 2010jl. It shows the distribution of mass-loss and wind velocity derived from different types of massive stars. One can see that all three objects lay within ranges of LBV giant eruptions but are not consistent with normal stellar winds.

With such high mass-loss rates, the most likely progenitor for ASASSN-15ua is probably an LBV or another object that experienced an LBV-like eruption (Smith & Owocki 2006; Gal-Yam et al. 2007; Smith & McCray 2007; Smith et al. 2007, 2010a). This progenitor likely had a series of eruptive outbursts or violent binary interaction (Smith & Arnett 2014), expelling a large amount of mass into the circumstellar environment.

An eruptive mechanism would be further validated by a well-resolved P Cygni profile in the day 175 spectrum. If the higher velocity seen in the P Cyg absorption on day 175 is real, that would suggest there is faster pre-shock material along our line of sight. Since the shock has expanded to larger radii in the CSM at this later time, this may suggest that the pre-SN mass-loss was not characterized by a constant velocity wind, but rather an impulsive

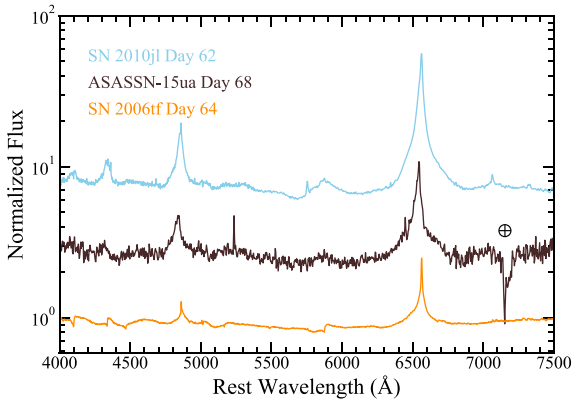

Figure 12. Spectra of ASASSN-15ua, SN2010jl (Smith et al. 2011b), and SN2006tf (Smith et al. 2008b) at a similar epoch (68, 62, and 64 d, respectively). All spectra have been corrected for extinction, using $E(B-V) = 0.0247$ mag for AASSN-15ua (see above), 0.027 mag for SN 2006tf (Smith et al. 2008b), and 0.024 mag for SN 2010jl (Jencson et al. 2016).

LBV-like explosion. A similar effect was seen in the case of SN 2006gy, where the increasing CSM speed encountered by the shock at later times outlined a Hubble-like flow, which in turn suggested that the pre-SN mass-loss occurred in a single major eruptive burst 8 yr before the SN, rather than a steady wind (Smith et al. 2010b). Alternatively, the increasing and broader P Cygni absorption may be similar to the case of SN 2017hcc, where higher resolution echelle spectra document the absorption profiles in greater detail, and provide evidence that the changes in line of sight absorption might be related to a bipolar geometry in the CSM shell (Smith & Andrews 2020).

4.2 Line asymmetry and possible dust formation

ASASSN-15ua's Hα emission becomes progressively more blueshifted with time, as discussed above and illustrated in Fig. 6. The three-Gaussian function centred at 0 km s^{-1} tends to overestimate flux on the red side of the line for each epoch. The asymmetry is most pronounced in the intermediate widths of the lines. Another view of this effect is shown in Fig. 8, where the difference between the reflected blue side (grey) and the red flux (black) grows with time. Note that because of the substantial redshift of ASASSN-15ua, there is a telluric feature near -4000 km s^{-1}, so the difference between the two sides is actually larger than inferred from this figure.

The asymmetry seen in the line profile is consistent with dust formation, where the newly formed dust in the SN ejecta or in the post-shock CDS causes selective extinction that blocks light from the far side of the SN more than the near side, thus preferentially suppressing redshifted emission in line profiles. Our spectral observations did not capture IR wavelengths, so it is unknown if ASASSN-15ua also had an IR excess. Additionally, the relatively low signal-to-noise ratio for the Hβ line and lack of IR spectra made it difficult to determine if the red-wing suppression exhibits a wavelength dependence, as seen in previous examples like SN 2010jl (Smith et al. 2012; Gall et al. 2014) and SN 2017hcc (Smith & Andrews 2020). However, as seen in Fig. 13, which places ASASSN-15ua in context with SN 2006tf and SN 2010jl, all SNe show similar asymmetric spectral evolution. Notably, ASASSN-15ua has only a mild red flux deficit like SN 2006tf, whereas the symmetry seen in Hα emission of SN 2010jl is much more extreme. Following the interpretation discussed for several previous SNe, it is likely that dust formation occurred primarily in the post-shock gas, since the majority of the asymmetry

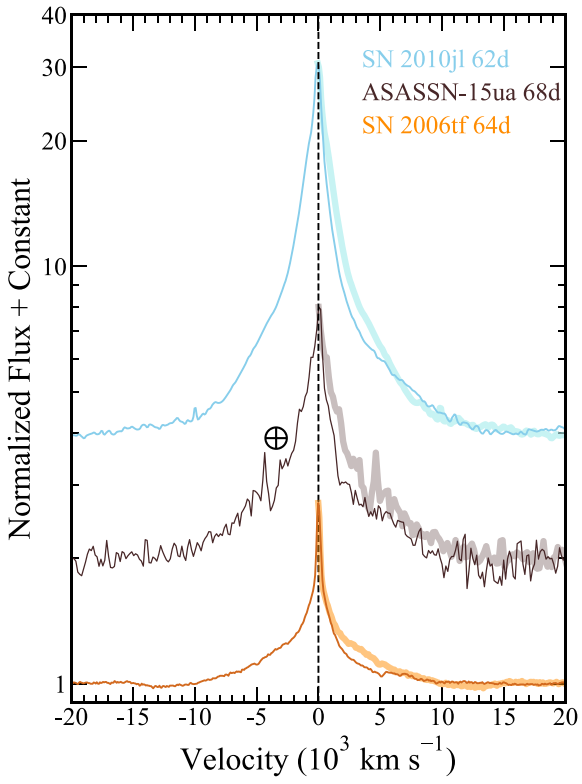

Figure 13. Spectra of ASASSN-15ua, SN2010jl, and SN2006tf at similar epochs (68, 62, and 64 d, respectively) enlarged around Hα, superimposed and shown with their blueshifted side reflected to the red side as in Fig. 8. The thicker and fainter tracing is the reflected blueshifted wing for each SN.

occurred in the intermediate-width component of the H emission. In ASASSN-15ua, the broad Hα component from the fast SN ejecta did not exhibit such a strong deficit of emission on the red wing.

Dust formation obviously impacts the colour of ASASSN-15ua; however, the decay rate of the light curve is heavily dominated by the density profile of the CSM, which is difficult to constrain in this study. Additionally, the quality and sampling of the light curves collected during time periods when spectra show evidence of dust formation is not sufficient for analysis, so we therefore do not use the light curve to infer properties of the dust formed in the CDS.

In principle, a blueshifted line shape may also be indicative of asymmetric CSM or an asymmetric explosion. The asymmetry would need to be a non-axisymmetric distribution (i.e. one-sided) in order to produce an asymmetric line as observed, with the bulk of the CSM on the near side of the SN. If the asymmetric lines are due to asymmetric CSM, then one would expect a random orientation of that one-sided CSM due to randomized viewing angles, and we should see roughly equal numbers of blueshifted and redshifted asymmetry in SNe IIn. While a non-axisymmetric feature is rarely observed as redshifted emission lines (Bilinski et al. 2018), the blueshifting as observed here is much more common. Moreover, in a SLSN IIn where the luminosity is dominated by CSM interaction, the emission from the fast SN ejecta is likely powered by back-illumination from the forward shock (Smith et al. 2008b); this is especially true at later epochs. However, if the CSM were one-sided, then we would expect to also see blueshifted asymmetry in the fast SN ejecta of ASASSN-15ua, but this is not observed. And finally, the narrow emission components appear to be centred

at zero velocity, arguing against a strongly one-sided distribution of CSM. We confirm that the CSM around ASASSN-15ua is at least axisymmetric, since the narrow and broad components are symmetric at all times. Although we cannot conclusively rule out aspherical CSM, the progressive blueshifting over time is most likely indicative of dust formation. As in the case of SN 2017hcc (Kumar et al. 2019), spectropolarimetry would have allowed us to further constrain the geometry of the CSM surrounding ASASSN-15ua.

Moreover, ASASSN-15ua shows the classic asymmetric evolution of SNe IIn, as seen in SN 2006tf (Smith et al. 2008b) and SN 2010jl (Smith et al. 2011b; Gall et al. 2014), as well as SN 2017hcc (IIn, Smith & Andrews 2020) and SN 2006jc (Ibn, Smith, Foley & Filippenko 2008a). Dust evidently began to form in the post-shock gas by around ≥48 d after explosion; there is some uncertainty is this estimate, since the time of explosion relative to the day of discovery is unknown. SN 2010jl (100d), SN 2017hcc (50-100d), and SN 2006jc (50-75d) formed dust in this region at a similar epoch.

4.3 An intermediate case between SN2006tf and SN2010jl

Fig. 12 compares spectra at similar epochs of SN 2006tf, SN 2010jl, and ASASSN-15ua. At ∼60 d, electron scattering no longer dominates the Hα line profile for all these three SNe. Each object seems to show a slight asymmetry in H α, H β, and even H γ line profiles. Most notably, SN 2010jl and SN 2006tf, as well as ASASSN-15ua, have extremely similar spectra at an epoch when the CSM is optically thin, so the underlying ejecta are observable, despite having dramatically different photometric and spectroscopic evolution.

This is also very apparent in Fig. 13, which compares the line profile of ASASSN-15ua to that of the other two SLSNe IIn. While the line asymmetry in ASASSN-15ua is mild, it is quite similar to the asymmetry seen in both of the two comparison SLSNe IIn at similar phases. We note that in the case of SN 2010jl, the blueshifted asymmetry became progressively significant at a much more dramatic pace at late times (Smith et al. 2012; Gall et al. 2014). The blueshifted asymmetry was not as pronounced in SN 2006tf (Smith et al. 2008b), even at late times. For ASASSN-15ua, we do not have comparable late-time spectra, but its overall spectral evolution shows a close resemblance to SN 2006tf.

Because of similarities in photometric and spectroscopic evolution between ASASSN-15ua and SN 2006tf, it is unsurprising that its precursor mass-loss history is more similar to SN 2006tf than SN 2010jl. ASASSN-15ua lost mass faster than SN 2010jl, which spent 30 yr losing a total of $3M_{\odot}$ (Fransson et al. 2014). Instead, it is more like SN 2006tf, which spent 20 yr losing a total of $\geq 18M_{\odot}$ (Smith et al. 2008b). The total mass lost by ASASSN-15ua is intermediate between SN 2010jl and SN 2006tf.

Both progenitors of SN 2006tf and SN 2010jl were proposed to have been LBVs or LBV-like eruptive massive stars, and the strong episodic mass-loss of ASASSN-15ua places its progenitor in the same parameter space. Our study of ASASSN-15ua indicates that there is a large, continuous range of mass ejection behaviours in these dying massive stars, as discussed below. The total ejected mass can range from 3 to $25M_{\odot}$, after comparing these three SNe IIn alone.

An alternative progenitor scenario is a red supergiant (RSG). In SN 2010jl, the trough of the P Cygni profile was 28 km s^{-1}, which would be consistent with an RSG-like wind. It is important to note, however, that this is 28 km s^{-1} CSM moving along the line of sight. Most of the outflow emission components were broader than this value (narrow H α emission showed a width of 120 km s^{-1}; Smith et al. 2011b, 2012). Since the outflow along our line of sight is substantially different from the bulk expansion speed indicated by isotropic emission, this requires an asymmetric CSM geometry. An outflow speed of 120 km s^{-1} is much faster than expected for a RSG wind. Since these outbursts can lift several solar masses of material off of the star, any RSG progenitor of a SN IIn must be at the extreme end of the ZAMS mass range (see Smith, Hinkle & Ryde 2009a).

Assuming a CSM radius of a few $\times$ 10^{15}cm, the densities (and mass-loss event time-scales) of SN 2006tf, SN 2010jl, and ASASSN-15ua are 0.5–9 $\times$ 10^{-10} g cm^{-3} (20 yr), 0.4 $\times$ 10^{-10} g cm^{-3} (30 yr), and 1–3 $\times$ 10^{-10} g cm^{-3} (12 yr). For both SN 2006tf and ASASSN-15ua, the wind density increased closer to the time of explosion. These values are calculated assuming an isotropic, spherical wind. However, the circumstellar environment observed around LBVs in the MW, LMC, and SMC are often bipolar (Smith et al. 2003, see also Smith & Andrews 2020), so an isotropic density measurement is likely not a fair metric of the diversity in mass-loss properties among these three objects.

As discussed by previous studies (for reviews, see Smith 2014, 2017), there are a few potential mechanisms to power these pre-SN mass-loss events.

The pulsational-pair instability (PPI) could drive extreme mass-loss, and this mechanism requires a progenitor mass of 100–150 $M_{\odot}$ (Woosley, Blinnikov & Heger 2007). The time-scale between the last pulse and explosion is highly sensitive to the He core mass with a range of $t = 10^{-3}$ to 10^{4} yr (Woosley 2017; Leung, Nomoto & Blinnikov 2019). The mass-loss inferred for ASASSN-15ua is consistent with this range, thus is consistent with PPI. The progenitor of SN 2010jl was estimated to be at least 30 $M_{\odot}$ based on the colour of its nearby stellar population. A potential difficulty for explaining ASASSN-15ua with this mechanism is that the high velocities seen in the wings of H α imply the presence of fast SN ejecta, while models of pulsational-pair events typically predict slower bulk expansion speeds around 2000 km s^{-1} (Woosley & Smith 2022).

Energy deposited into the stellar envelope via wave-driving (Shiode & Quataert 2014; Fuller 2017; Wu & Fuller 2021) is consistent with the CSM kinetic energy inferred here for ASASSN-15ua. However, the duration of extreme mass-loss exceeds the ∼1 yr duration of Ne and O burning (and far exceeds the ∼days of Si burning) that fuels wave-driven mass-loss.

The stellar envelope could potentially also become unbound due to a pulsation driven by convective turbulence or explosive burning (Smith & Arnett 2014). Energetic pulsations could unbind the remaining H envelope on their own, or sub-binding energy pulsations could be assisted by the progenitor's near-Eddington luminosity to remove the envelope. Lower-energy pulsations or pre-SN swelling of the star's envelope could kick-start mass transfer if the progenitor evolved in close separation to a companion.

In fact, binary interaction is likely to influence or to be responsible for these mass-loss events (Chevalier 2012; Smith 2014; Smith & Arnett 2014). Many (2/3 to 3/4 of the population) massive stars in binary systems will interact over the course of their lifetime (Sana et al. 2012; Moe & Di Stefano 2017), whereas a small subset of these would need to be experiencing that interaction shortly before explosion in order to produce the nearby dense CSM required for SNe IIn (Smith & Arnett 2014). RLOF and common envelope phases are poorly understood, and the luminosity of progenitors of SNe IIn may approach the Eddington limit, so binary interaction or stellar envelope instabilities may be greatly emphasized. ASASSN-15ua sheds light on the continuum that exists between these behaviours, and suggests that whatever mechanism powers the pre-SN mass-loss in SLSNe IIn should accommodate a wide and continuous range of mass, energy, and pre-SN time-scales.

5 CONCLUSION

Our analysis of ASASSN-15ua provides critical insight to the underlying mechanisms driving eruptive mass-loss in extremely massive stars and probes the physics of interacting SLSNe. Enumerated below is a summary of this study:

(i) The superluminous SN IIn, ASASSN-15ua, radiated at least 3×10^{50} erg. This is an underestimate since the rise to peak and a BC were not accounted for. This value approaches the canonical energy of a typical core-collapse SN, $\sim 10^{51}$ erg, suggesting the mechanism behind its extreme luminosity is shock–CSM interaction.

(ii) The progenitor of ASASSN-15ua suffered extreme mass-loss for at least 12 yr prior to the SN with a steady rate of 0.4 $M_\odot$ yr^{-1}, and this rate increased to 0.7 $M_\odot$ yr^{-1} at about 4.5 yr prior to SN. The total mass of this CSM is at least 6 $M_\odot$, imparted with 6×10^{47} erg of kinetic energy. This mass-loss was due to an eruptive mechanism, and not a normal line-driven stellar wind.

(iii) It is likely that the progenitor of ASASSN-15ua was an LBV or some similar type of unstable supergiant that cataclysmically lost its H envelope mass, perhaps via binary interaction or pulsational pair instability.

(iv) ASASSN-15ua shows the classic dust formation evolution of SNe IIn, where dust began to form in the post-shock gas at most 48 d after discovery and began to block light from the receding portions of the SN, thereby suppressing the redshifted wings of emission lines. This provides additional evidence that radiative cooling in this thin, clumpy region is highly efficient, enabling dust to form.

(v) ASASSN-15ua is an intermediate case between SN 2006tf and SN 2010jl in a number of its measurable properties. ASASSN-15ua's spectral evolution and photometric evolution resemble that of SN 2006tf more closely, while its mass-loss history and continuum evolution are more comparable to SN 2010jl. A similar mechanism may power these objects, being able to produce a range of mass, energy, and timecales in pre-SN mass-loss.

DATA AVAILABILTY

The data underlying this article will be shared on reasonable request to the corresponding author.

ACKNOWLEDGEMENTS

We thank an anonymous referee for helpful comments that improved this manuscript. We thank K. Weil and B. Subrayan for helpful guidance and discussion as well as B. Lewis for incredible advice in the development of this work. DM acknowledges NSF support from grants PHY-1914448, PHY-2209451, AST-2037297, and AST-2206532. We wish to extend a special thanks to those of Tohono O'odham ancestry on whose sacred mountain we are privileged to be guests.

Observations reported here were obtained at the MMT Observatory, a joint facility of the University of Arizona and the Smithsonian Institution. Observations using Steward Observatory facilities were obtained as part of the observing programme AZTEC: Arizona Transient Exploration and Characterization, which received support from NSF grant AST-1515559. This work was supported through a NASA grant awarded to the Arizona/NASA Space Grant Consortium and by the Rolf Scharenberg Graduate Summer Research Fellowship. Support was also provided by the National Aeronautics and Space Administration (NASA) through HST grant AR-14316 from the Space Telescope Science Institute, operated by AURA, Inc., under NASA contract NAS5-26555. Some data reported here were obtained at the MMT Observatory, a joint facility of the University of Arizona and the Smithsonian Institution.

This work is supported by the international Gemini Observatory, a programme of NSF's NOIRLab, which is managed by the Association of Universities for Research in Astronomy (AURA) under a cooperative agreement with the National Science Foundation, on behalf of the Gemini partnership of Argentina, Brazil, Canada, Chile, the Republic of Korea, and the United States of America.

CDK was supported in part by a CIERA postdoctoral fellowship.

Facilities: MMT (Bluechannel), SO: Bok (B&C), SO: Super-LOTIS.

REFERENCES

Angel J. R. P., Hilliard R. L., Weymann R. J., 1979, in Weekes T. C., ed., The MMT and the Future of Ground-Based Astronomy. Mount Hopkins Observatory, Arizona, p. 87
Bevan A. et al., 2019, MNRAS, 485, 5192
Bevan A. M. et al., 2020, ApJ, 894, 111
Bilinski C., Smith N., Li W., Williams G. G., Zheng W., Filippenko A. V., 2015, MNRAS, 450, 246
Bilinski C. et al., 2018, MNRAS, 475, 1104
Challis P., Johnson S., Kirshner R., Falco E., Berlind P., Prieto J. L., Stanek K. Z., 2015, Astron. Telegram, 8410, 1
Chambers K. C. et al., 2016, preprint (arXiv:1612.05560)
Chevalier R. A., 2012, ApJ, 752, L2
Chevalier R. A., Irwin C. M., 2011, ApJ, 729, L6
Chugai N. N., 2001, MNRAS, 326, 1448
Elias-Rosa N. et al., 2016, MNRAS, 463, 3894
Fabricant D. et al., 2019, PASP, 131, 075004
Filippenko A. V., 1997, ARA&A, 35, 309
Flewelling H. A. et al., 2020, ApJS, 251, 7
Fontaine G., Green E., Charpinet S., Latour M., Randall S., Van Grootel V., Brassard P., 2014, in van Grootel V., Green E., Fontaine G., Charpinet S.eds, ASP Conf. Ser. Vol. 481, 6th Meeting on Hot Subdwarf Stars and Related Objects. Astron. Soc. Pac., San Francisco, p. 19
Fransson C. et al., 2014, ApJ, 797, 118
Fraser M. et al., 2013, ApJ, 779, L8
Fuller J., 2017, MNRAS, 470, 1642
Fuller J., Ro S., 2018, MNRAS, 476, 1853
Gal-Yam A., 2012, Science, 337, 927
Gal-Yam A. et al., 2007, ApJ, 656, 372
Gall C. et al., 2014, Nature, 511, 326
Garretson B., 2021, Catalog of over ten thousand SN-like light curves from ZTF, Zenodo
Hart K. et al., 2023, preprint (arXiv:2304.03791)
Jencson J. E., Prieto J. L., Kochanek C. S., Shappee B. J., Stanek K. Z., Pogge R. W., 2016, MNRAS, 456, 2622
Kasen D., Bildsten L., 2010, ApJ, 717, 245
Kilpatrick C. D., Andrews J. E., Smith N., Milne P., Rieke G. H., Zheng W., Filippenko A. V., 2016, MNRAS, 463, 1088
Kumar B. et al., 2019, MNRAS, 488, 3089
Leung S.-C., Nomoto K., Blinnikov S., 2019, ApJ, 887, 72
Maeda K. et al., 2007, ApJ, 666, 1069
Magnier E. A. et al., 2020, ApJS, 251, 6
Masi G. et al., 2015, Astron. Telegram, 8408, 1
Moe M., Di Stefano R., 2017, ApJS, 230, 15
Niculescu-Duvaz M. et al., 2022, MNRAS, 515, 4302
Ofek E. O. et al., 2014, ApJ, 789, 104
Pastorello A. et al., 2007, Nature, 447, 829
Poznanski D., Prochaska J. X., Bloom J. S., 2012, MNRAS, 426, 1465
Quataert E., Shiode J., 2012, MNRAS, 423, L92
Quimby R., Castro F., Mondol P., Caldwell J., Terrazas E., 2007, Central Bureau Electronic Telegrams, 793, 1
Quimby R. M. et al., 2011, Nature, 474, 487

Renzo M., Farmer R., Justham S., Götberg Y., de Mink S. E., Zapartas E., Marchant P., Smith N., 2020, A&A, 640, A56
Sana H. et al., 2012, Science, 337, 444
Schlafly E. F., Finkbeiner D. P., 2011, ApJ, 737, 103
Schlafly E. F. et al., 2012, ApJ, 756, 158
Schlegel E. M., 1990, MNRAS, 244, 269
Schrøder S. L., MacLeod M., Loeb A., Vigna-Gómez A., Mandel I., 2020, ApJ, 892, 13
Shappee B. J. et al., 2014, ApJ, 788, 48
Shiode J. H., Quataert E., 2014, ApJ, 780, 96
Smith N., 2014, ARA&A, 52, 487
Smith N., 2017, in Alsabti A. W., Murdin P., Interacting Supernovae: Types IIn and Ibn. Springer, Cham, United States, p. 403
Smith N., Andrews J. E., 2020, MNRAS, 499, 3544
Smith N., Arnett W. D., 2014, ApJ, 785, 82
Smith N., McCray R., 2007, ApJ, 671, L17
Smith N., Owocki S. P., 2006, ApJ, 645, L45
Smith N., Davidson K., Gull T. R., Ishibashi K., Hillier D. J., 2003, ApJ, 586, 432
Smith N. et al., 2007, ApJ, 666, 1116
Smith N., Foley R. J., Filippenko A. V., 2008a, ApJ, 680, 568
Smith N., Chornock R., Li W., Ganeshalingam M., Silverman J. M., Foley R. J., Filippenko A. V., Barth A. J., 2008b, ApJ, 686, 467
Smith N., Hinkle K. H., Ryde N., 2009a, AJ, 137, 3558
Smith N. et al., 2009b, ApJ, 695, 1334
Smith N. et al., 2010a, AJ, 139, 1451
Smith N., Chornock R., Silverman J. M., Filippenko A. V., Foley R. J., 2010b, ApJ, 709, 856
Smith N., Li W., Silverman J. M., Ganeshalingam M., Filippenko A. V., 2011a, MNRAS, 415, 773
Smith N. et al., 2011b, ApJ, 732, 63
Smith N., Silverman J. M., Filippenko A. V., Cooper M. C., Matheson T., Bian F., Weiner B. J., Comerford J. M., 2012, AJ, 143, 17
Smith N., Mauerhan J. C., Prieto J. L., 2014, MNRAS, 438, 1191
Smith N. et al., 2018, MNRAS, 480, 1457
Smith N., Andrews J. E., Filippenko A. V., Fox O. D., Mauerhan J. C., Van Dyk S. D., 2022, MNRAS, 515, 71
Stoll R., Prieto J. L., Stanek K. Z., Pogge R. W., Szczygieł D. M., Pojmański G., Antognini J., Yan H., 2011, ApJ, 730, 34
Tonry J., Onaka P., Luppino G., Isani S., 2006, in Ryan S., The Advanced Maui Optical and Space Surveillance Technologies Conference. The Maui Economic Development Board, Wailea, Maui, Hawaii, United States, p. E47
van Dyk S. D., 2005, in Humphreys R., Stanek K.eds, ASP Conf. Series Vol. 332, The Fate of the Most Massive Stars. Astron. Soc. Pac., San Francisco, p. 49
van Marle A. J., Smith N., Owocki S. P., van Veelen B., 2010, MNRAS, 407, 2305
Williams G. G., Milne P. A., Park H. S., Barthelmy S. D., Hartmann D. H., Updike A., Hurley K., 2008, in Galassi M., Palmer D., Fenimore E.eds, AIP Conf. Proc. Vol. 1000, Gamma-Ray Bursts 2007. Am. Inst. Phys., New York, p. 535
Woosley S. E., 2010, ApJ, 719, L204
Woosley S. E., 2017, ApJ, 836, 244
Woosley S. E., Smith N., 2022, ApJ, 938, 57
Woosley S. E., Blinnikov S., Heger A., 2007, Nature, 450, 390
Wright E. L., 2006, PASP, 118, 1711
Wu S., Fuller J., 2021, ApJ, 906, 3
Zhang T. et al., 2012, AJ, 144, 131

This paper has been typeset from a TEX/LATEX file prepared by the author.